# Porous Ir-Sn Binary Oxide Nanorod Assembly as an Efficient Electrocatalyst for Water Oxidation

*Wangting Lu[1], Peng Yuan[2], Feng Wei[1], Kun Cheng[1], Wenhui Li[1], Youhua Zhou[1], Wanquan Zheng[1], Geng Zhang[2,*]*

[1] Institute for Interdisciplinary Research, Jianghan University, 430056, Wuhan, P. R. China.
[2] Department of Chemistry, College of Science, Huazhong Agricultural University, 430070, Wuhan, P. R. China.
[*]E-mail: zhanggeng@mail.hzau.edu.cn

The large-scale deployment of proton exchange membrane water electrolysis technologies is hindered by the usage of high-cost and scarce noble metal oxides as catalysts for the oxygen evolution reaction (OER) at an anode. Herein, we provided a facile method to synthesize Ir-Sn binary oxides in the form of a nanorod assembly with a large number of pores and a lower Ir content as efficient catalysts for the OER. The deep eutectic solvent formed by glucose and urea plays a crucial role in the synthesis. When heating the deep eutectic solution containing $IrCl_3$ and $SnCl_2$ at 180°C, the polymerization and the following expansion of glucose produces a bread-like porous foam with embedded Ir and Sn metal ions. During the following calcination process in Ar and air, the sintering of the catalyst is inhibited owing to the blocking effect of the glucose-derived carbonaceous material, and the removal of the carbonaceous species produces pores in the final product. The $-NH_2$ groups in urea can form complexes with the Ir and Sn metal ions, which is beneficial to to obtain the formation of an Ir-Sn binary oxide with uniform composition. As a result, an Ir-Sn oxide with an Ir/Sn molar ratio at 2/1 presents the best catalytic activity for the OER among the Ir-Sn oxides, which is almost identical to that of a mono-Ir oxide. The method in this work provided a pathway to fabricate high-performance OER catalysts with low Ir content.

## 1. INTRODUCTION

Splitting water through electrolysis by using renewable energy (*e.g.*, solar and wind energy) is an efficient and clean pathway to achieve high-quality hydrogen.[1, 2] In comparison with conventional water electrolysis in an alkaline liquid electrolyte, water electrolysis based on a solid polymer electrolyte (*e.g.*, proton exchange membrane, PEM) provides some advantages, such as better reliability, safer operation, and a higher working current density. [3] Even so, the key factor in

determining whether water electrolysis technology can be widely used is the energy consumption, *i.e.*, the cell voltage must be decreased as much as possible. The cell voltage of a water electrolyzer largely depends on the overpotential of the hydrogen evolution reaction (HER) at the cathode and the oxygen evolution reaction (OER) at the anode of the electrolyzer. Under the acidic environment in a PEM water electrolyzer, the overpotential of OER is much higher than that of HER.[3, 4] Therefore, it is highly important to develop an efficient OER electrocatalyst to decrease its overpotential.

Currently, the common electrocatalysts used to accelerate OER kinetics are based on $IrO_2/RuO_2$, in which $IrO_2$ has better stability.[3, 5] However, the high cost and scarcity of noble metals are undoubtedly obstacles for the large-scale deployment of water electrolysis technologies. Therefore, it is greatly attractive to develop efficient water-splitting OER electrocatalysts with earth-abundant elements. However, in acidic environments, $IrO_2$ and $RuO_2$ are still indispensable; thus, it is highly necessary to increase the utilization of elemental Ir/Ru in the catalyst.[6, 7] It has been reported that loading Ir/Ru oxide on a noble-metal free and acid-resistant oxide support (*e.g.*, $TiO_2$,[8, 9] $SnO_2$,[10-13] $Ta_2O_5$[14]) helps increase its dispersion, but the low conductivity of these transition metal oxides is adverse to the activity of Ir/Ru oxide. Alternatively, the direct introduction of earth-abundant elements into the Ir/Ru oxide is an effective strategy to increase the utilization of elemental Ir/Ru; moreover, the conductivity of the catalyst can be largely maintained due to the presence of the highly conductive Ir/Ru oxide in the composite.[15, 16] The common methods for the preparation of powder composite catalysts of Ir/Ru and transition metal oxides include the Adams-fusion,[16] sol-gel[17] and colloidal methods[15, 18, 19]. However, it is difficult to avoid the sintering of the catalyst during high-temperature treatment in the above methods. In contrast, other strategies such as a template-assisted synthesis method is helpful to reduce the sintering of the catalyst.[20-22] Nevertheless, the complicated preparation procedure (*e.g.*, the synthesis and removal of templates) limits its wide application. Therefore, it is significant to develop a facile and efficient method to prepare the composite oxide of Ir/Ru and earth-abundant metal oxides.

Herein, we provided a facile method to synthesize Ir-Sn binary oxides in the form of a nanorod assembly with a large number of pores. The deep eutectic solvent prepared by glucose and urea is used to dissolve Ir and Sn salts. The glucose will expand remarkably to a bread-like foam when the mixture was heated at 180°C with embedded Ir and Sn metal ions. During the following calcination process, the sintering of the Ir and Sn species was decreased owing to the blocking effect of glucose-derived carbonaceous material, and the removal of the carbonaceous species will produce pores in the final product. The $-NH_2$ groups in urea can form complexes with Ir and Sn metal ions, which is beneficial for the formation of an Ir-Sn binary oxide with a uniform composition. As a result, the Ir-Sn oxide with an Ir/Sn molar ratio at 2/1 presented the best catalytic activity for the OER among the Ir-Sn oxides, which is almost identical to that of mono-Ir oxide.

## 2. EXPERIMENTAL SECTION

### 2.1 Electrocatalyst preparation

Typically, 6.0 g glucose and 4.0 g urea were mixed together and heated at 100°C until the mixture completely melted. Then, 3.965 mL $IrCl_3$ aqueous solution (113 mmol $L^{-1}$) together with a

given amount of $SnCl_2 \cdot 2H_2O$ powder with an Ir/Sn molar ratio at 2:1, 1:1 or 1:2 was added into this deep eutectic solvent. Subsequently, the solution was heated at 180°C for 12 h, during which the solution gradually transformed to a dark brown bread-like foam referred to as $Ir_m$-$Sn_n$-GF (G means glucose, F means foam and m/n is the molar ratio of Ir/Sn). $Ir_m$-$Sn_n$-GF was then crushed and ground thoroughly, followed by calcination at 500°C in air for 1 h. The final product was denoted as $Ir_mSn_nO_x$ with different Ir/Sn feed ratios. If $SnCl_2$ was removed, then the precursor and the final product were named Ir-GF and $IrO_x$, respectively.

As an improved preparation method, $Ir_m$-$Sn_n$-GF and Ir-GF were first heat treated at 500°C in an Ar atmosphere for 1 h. After that, the precursors were calcinated at 500°C in air to remove the carbonaceous species. The material correspondingly obtained were named $Ir_mSn_nO_x$-Ar and $IrO_x$-Ar, respectively.

## 2.2 Characterizations

The X-ray diffraction (XRD) patterns of samples were recorded on a Bruker D8 Advance X-ray diffractometer using Cu Kα radiation. Transmission electron microscopy (TEM) images were acquired with a JEOL JEM-1200EX microscope. The thermogravimetric (TG) analyses were conducted on a NETZSCH TG 209F3 TG analyzer under air flow.

## 2.3 Electrochemical measurements

The electrochemical performance of the samples were evaluated in a conventional three-electrode system connected by a CHI-660D electrochemical station (CH Instruments, Inc.) in 0.5 M $H_2SO_4$ at room temperature. A catalyst slurry was prepared by dispersing 10 mg of the catalyst in a mixture of 2 mL isopropanol and 50 μL 5% Nafion solution (Sigma-Aldrich) by sonication for 30 min. The working electrode was prepared by dipping 10 μL catalyst slurry onto a glassy carbon electrode (5 mm in diameter), followed by drying in air at room temperature. A Pt mesh and a saturated calomel electrode (SCE) were adopted as the counter electrode and reference electrode, respectively. All electrode potentials were given versus the reversible hydrogen electrode (RHE) unless otherwise noted.

The cyclic voltammetry (CV) curves were recorded at a scan rate of 50 mV s$^{-1}$. The OER polarization curves of the catalysts were acquired at a scan rate of 5 mV s$^{-1}$. The electrochemical impedance spectra (EIS) of catalysts were recorded at 1.4 V (vs. SCE) at a frequency range from $10^5$ Hz to 1 Hz.

## 3. RESULTS AND DISCUSSION

The preparation pathway of the $IrSnO_x$ nanorod assembly was illustrated in Figure 1. First, a deep eutectic solvent was prepared by heating the mixture of glucose and urea at 100°C, followed by the addition of $IrCl_3$ and $SnCl_2$. Then, the solution was heated at 180°C for 12 h in an oven, during

which glucose melted and polymerized through dehydration, and the polymerized glucose was blown into porous foam with the help of gas generated from the decomposition of urea and glucose.
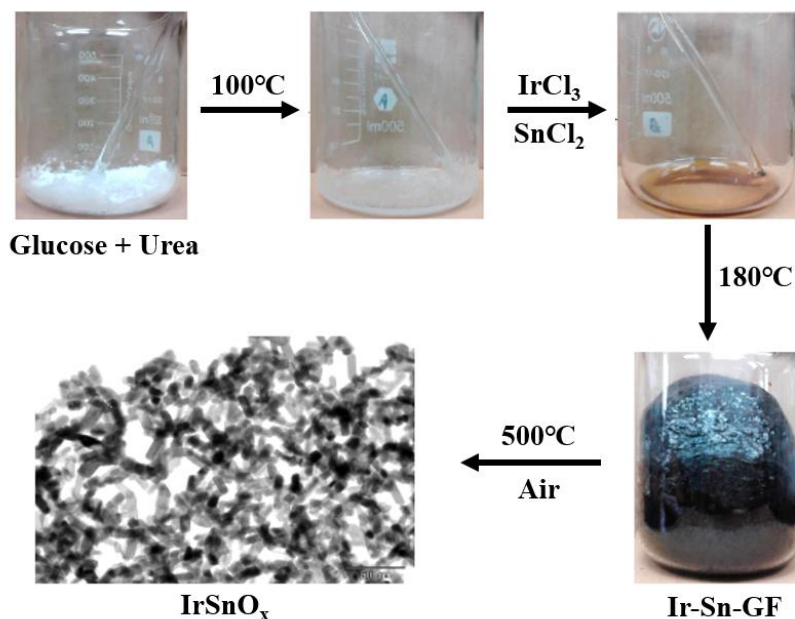


**Figure 1.** Schematic illustration of the preparation of electrocatalyst.

The dark brown foam ($Ir_m$-$Sn_n$-GF) was then heated in air at 500°C to remove the carbon, and the $Ir_mSn_nO_x$ nanorod assembly was finally obtained. To determine the time required to remove the carbonaceous species, TG analysis was carried out. The sample was heated to 500°C at a heating rate of 10°C min$^{-1}$ and then held at 500°C. As shown in Figure 2, the mixture starts to decompose at approximately 200°C. After staying at 500°C for more than 10 min, the sample weight was almost unchanged, indicating the complete removal of carbon in the mixture. To remove carbon completely, the time of calcination was chosen to be 60 min.
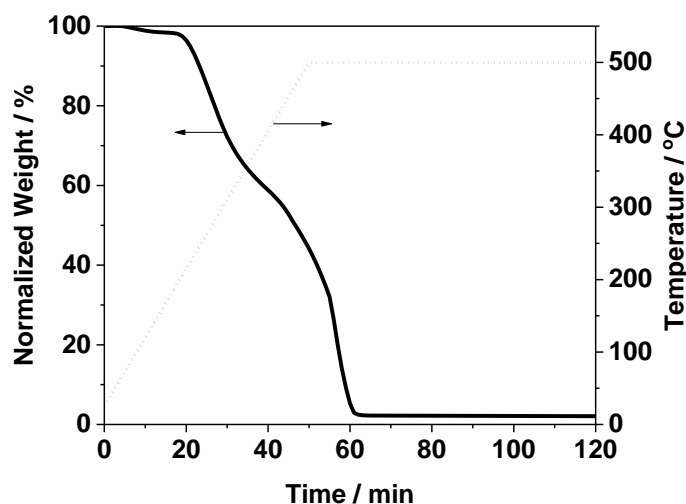


**Figure 2.** TG curves of $Ir_2$-$Sn_1$-GF in an air flow. The sample was first heated to 500°C at a heating rate of 10°C min$^{-1}$ and then held at 500°C.

The XRD patterns of $Ir_mSn_nO_x$ are presented in Figure 3. For $IrO_x$ without Sn, the peaks centered at 40.7°, 47.3°, 69.1°, 83.4° and 88.0° can be indexed to the (111), (200), (220), (311) and (222) crystalline planes of face-centered-cubic Ir (PDF# 06-0598), respectively. The weak peaks at 27.8° and 34.7° can be assigned to the (110) and (101) planes of $IrO_2$ (PDF# 15-0870), respectively. The XRD analysis illustrated that $IrO_x$ was composed of metallic Ir with a minute amount of $IrO_2$. When $SnCl_2$ was added, the peaks of $Ir_mSn_nO_x$ at approximately 27°, 34°, 39°, 47°, 53°, 58°, 65°, 69°, 72° and 83° ascribed to $SnO_2$ and/or $IrO_2$ were intensified remarkably in comparison with those of metallic Ir, indicating that the introduction of Sn promoted the formation of $IrO_2$.
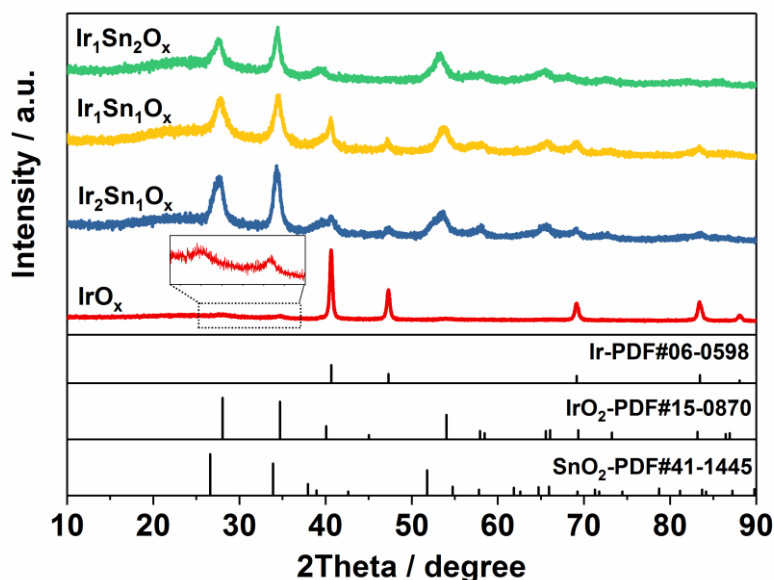


**Figure 3.** XRD patterns of $Ir_2Sn_1O_x$, $Ir_1Sn_1O_x$, $Ir_1Sn_2O_x$ and $IrO_x$.

The TEM images of $IrO_x$ and $Ir_mSn_nO_x$ are shown in Figure 4. As for $IrO_x$, nanorods with lengths of ~50 nm and diameters of ~8 nm were obtained. When $SnCl_2$ was added, the final products ($Ir_1Sn_2O_x$, $Ir_1Sn_1O_x$ and $Ir_2Sn_1O_x$) also presented a nanorod-like morphology. The nanorods connected to each other resulting in a porous assembly. It was found that the porosity of $Ir_mSn_nO_x$ was much higher than that of the Ir-based oxides synthesized by a simple pyrolysis method and usually highly sintered with a low porosity.[14, 15, 17] The porous $Ir_mSn_nO_x$ assembly was speculated to be generated by the following process. The polymerization and the following expansion of glucose gave rise to GF with a significant increase in volume. At the same time, the dispersion of $IrCl_3$ and $SnCl_2$ incorporated in the GF was increased. Moreover, the GF played a role as a physical barrier to protect the oxides from sintering during calcination, and the removal of GF produced pores in the final product. The – $NH_2$ groups in urea can form complexes with Ir and Sn metal ions during the GF formation, which will improve the composition uniformity of the Ir-Sn binary oxide. All the above aspects enhanced the electrochemical performance of the product.
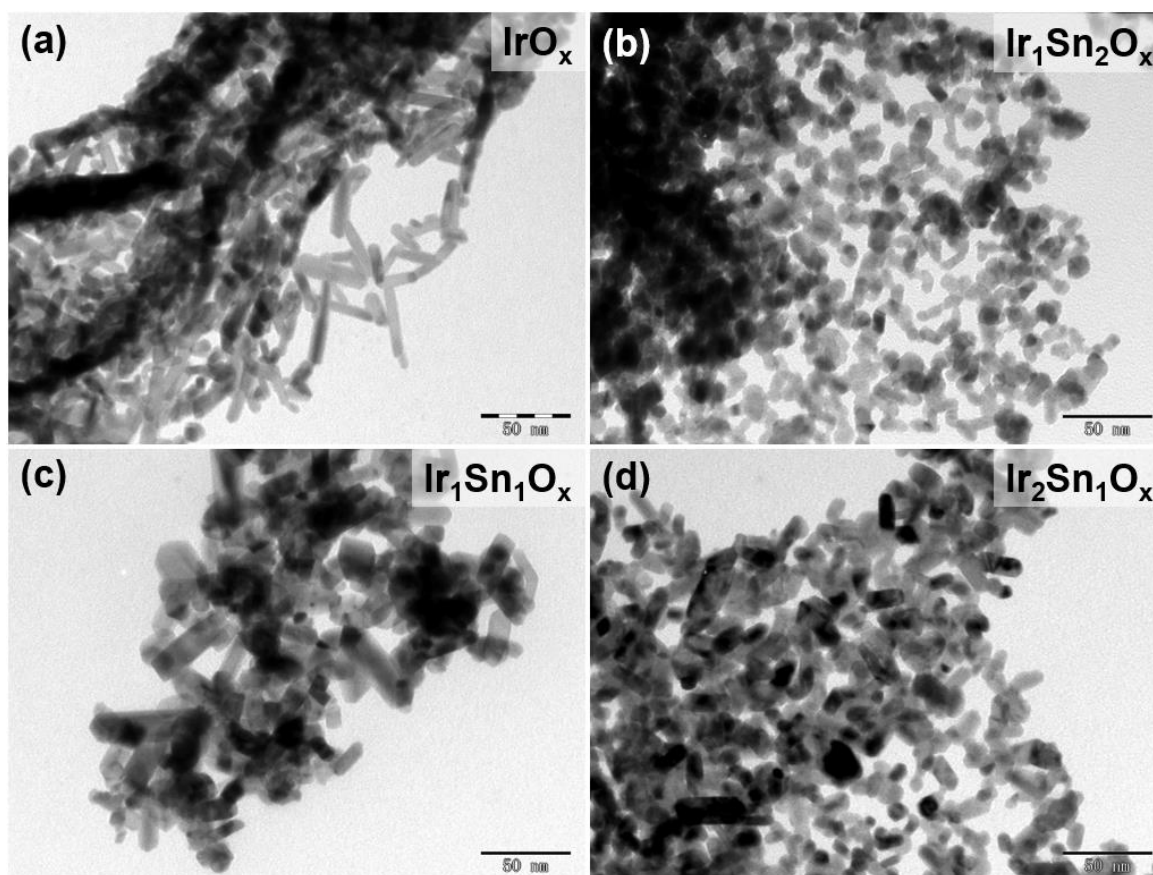
**Figure 4.** TEM images of (a) $IrO_x$, (b) $Ir_1Sn_2O_x$, (c) $Ir_1Sn_1O_x$ and (d) $Ir_2Sn_1O_x$.

The CV curves of $IrO_x$ and $Ir_mSn_nO_x$ are shown in Figure 5a. The peaks centered at ~0.8 V and ~1.1 V come from the $Ir^{3+}/Ir^{4+}$ and $Ir^{4+}/Ir^{6+}$ redox states, respectively.[23] It is well accepted that the charge ($Q$) calculated from the area inside the CV curve is positively correlated with the active area of the electrocatalyst (Equation 1).

$$Q = \int_{E_1}^{E_2} \frac{j}{v} dE \tag{1}$$

where $E_1$ and $E_2$ are the low and high electrode potential of the integration area, respectively; $j$ is the current density (mA cm$^{-2}$); $v$ is the scan rate (V s$^{-1}$); and $E$ is the electrode potential. Herein, $Q$ reflects the amount of $IrO_2$ on the surface of the sample. The area of $IrO_x$ ($Q = 1.90$ mC cm$^{-2}$) was small, probably due to the small amount of $IrO_2$ in the sample, which was indicated by XRD. The $Q$ of $Ir_1Sn_2O_x$ (3.31 mC cm$^{-2}$) was larger than that of $IrO_x$, and with an increase in the Ir/Sn molar ratio, the $Q$ values correspondingly increases to 6.56 and 8.23 mC cm$^{-2}$ for $Ir_1Sn_1O_x$ and $Ir_2Sn_1O_x$, respectively. The OER polarization curves of the four samples are displayed in Figure 5b. The current densities at 1.55 V for $Ir_2Sn_1O_x$, $Ir_1Sn_1O_x$, $Ir_1Sn_2O_x$ and $IrO_x$ were 1.2, 0.4, 0.04 and 0.6 mA cm$^{-2}$, respectively, of which $Ir_2Sn_1O_x$ demonstrated the best activity. Furthermore, the Tafel slopes of $Ir_2Sn_1O_x$, $Ir_1Sn_1O_x$ and $Ir_1Sn_2O_x$ were 65, 67 and 93 mV dec$^{-1}$, further proving the superior activity of $Ir_2Sn_1O_x$ towards the OER. EIS was used to measure the electron transfer resistance of the catalyst during oxygen evolution. As shown in Figure 5d, the electron transfer resistance ($R_{ct}$) decreased in the order of $Ir_1Sn_2O_x$ (996.7

ohm) > $Ir_1Sn_1O_x$ (54.91 ohm) > $IrO_x$ (55.46 ohm) > $Ir_2Sn_1O_x$ (36.48 ohm), which is consistent with the results shown in Figure 5b and 5c. The above results demonstrate that $Ir_2Sn_1O_x$ possessed the best activity among the Ir-Sn oxides, even higher than that of $IrO_x$, which may be due to the increased utilization of Ir atoms and a synergistic effect between the Ir and Sn species.[18, 23, 24]
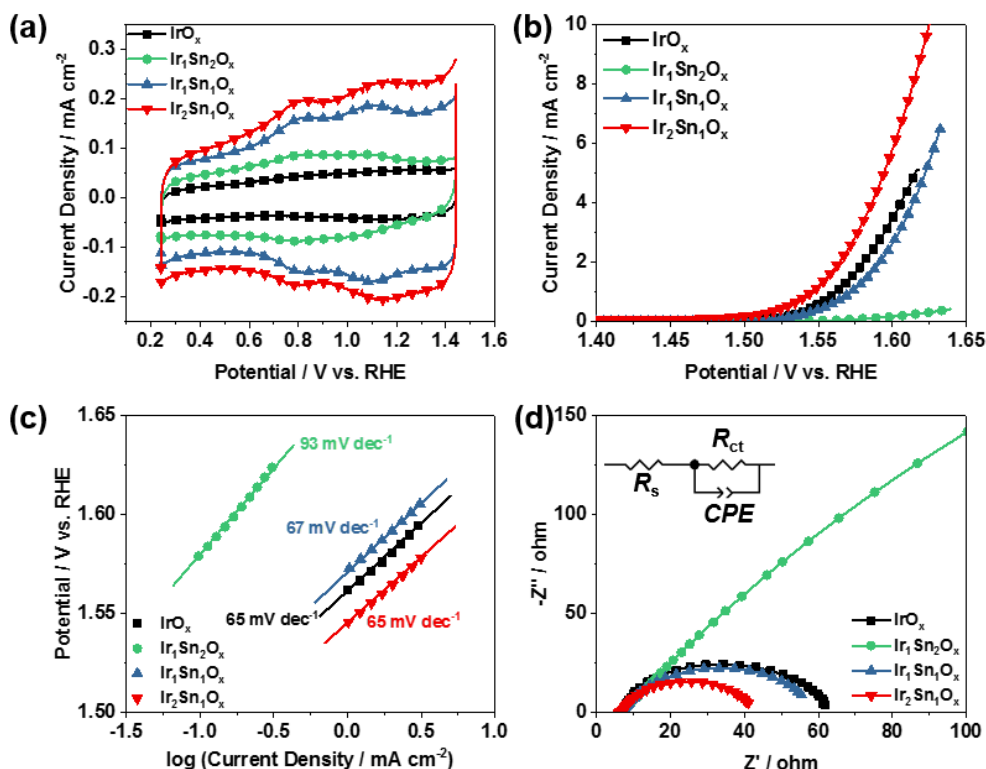


**Figure 5.** (a) CV curves, (b) OER polarization curves, (c) Tafel plots and (d) EIS spectra of $Ir_2Sn_1O_x$, $Ir_1Sn_1O_x$, $Ir_1Sn_2O_x$ and $IrO_x$ in 0.5 M $H_2SO_4$. The equivalent circuit of the EIS spectrum is shown in the inset of (d).
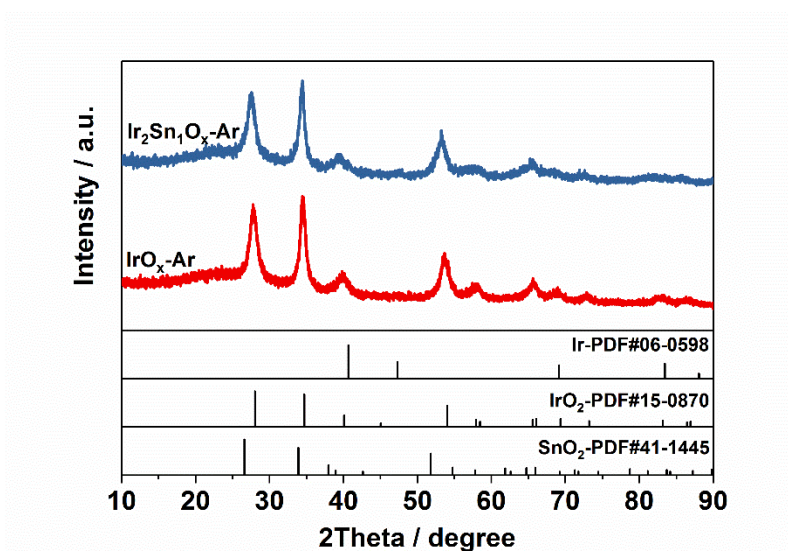


**Figure 6.** XRD patterns of $Ir_2Sn_1O_x$-Ar and $IrO_x$-Ar.

To further increase the interaction between the Ir and Sn species in $Ir_2Sn_1O_x$, the $Ir_2$-$Sn_1$-GF precursor was first treated at 500°C in Ar atmosphere before the removal of the carbonaceous species, and the final product was denoted as $Ir_2Sn_1O_x$-Ar. For comparison, the Ir-GF precursor was also treated by the same process, and $IrO_x$-Ar was obtained. As shown in Figure 6, $IrO_x$-Ar shows a series of diffraction peaks that correspond to $IrO_2$, and the peaks from metallic Ir were almost negligible, which is in sharp contrast to that of $IrO_x$ (Figure 3). Similarly, $Ir_2Sn_1O_x$-Ar also shows an $IrO_2$/$SnO_2$ pattern. The above results indicated that treatment at 500°C in Ar facilitated the formation of metal oxides. The TEM images of $IrO_x$-Ar and $Ir_2Sn_1O_x$-Ar (Figure 7) demonstrate that the porous nanorod assembly is also obtained after Ar treatment, indicating that Ar treatment does not accelerate the sintering of metal oxides.
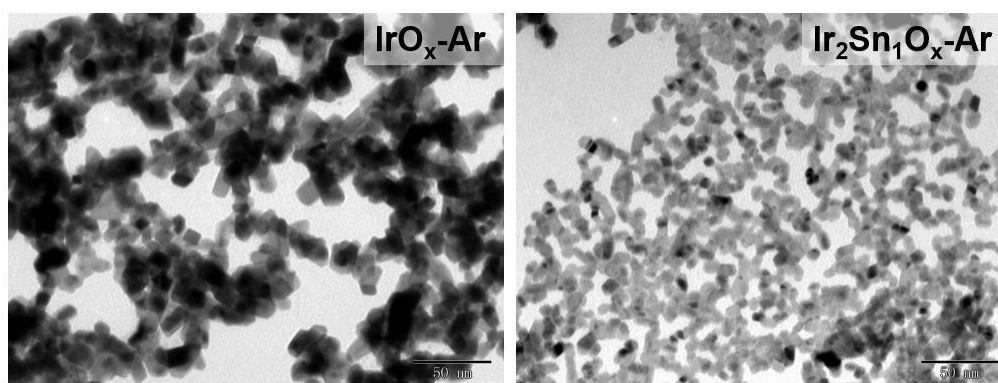


**Figure 7.** TEM images of (a) $IrO_x$-Ar and (b) $Ir_2Sn_1O_x$-Ar.

The electrochemical performance of $IrO_x$-Ar and $Ir_2Sn_1O_x$-Ar were evaluated (Figure 8). The $Q$ calculated from Equation 1 is 7.28 mC $cm^{-2}$ for $IrO_x$-Ar, which is much larger than that of $IrO_x$ (1.90 mC $cm^{-2}$) (Figure 8a), indicating that the electrochemical surface area of $IrO_x$-Ar was obviously enlarged in comparison with that of $IrO_x$ due to the increased amount of $IrO_2$ in $IrO_x$-Ar. This increase gave rise to an enhancement in the OER activity of $IrO_x$-Ar, *i.e.*, the current density at 1.55 V was 2.7 mA $cm^{-2}$ vs. 0.6 mA $cm^{-2}$ for $IrO_x$ (Figure 8b). Meanwhile, the Tafel slope for $IrO_x$-Ar was reduced from 65 mV $dec^{-1}$ ($IrO_x$) to 48 mV $dec^{-1}$ (Figure 8c) and $R_{ct}$ decreased from 55.46 ohm to 14.91 ohm (Figure 8d). Similarly, after treatment at 500°C in Ar, the oxygen evolution current at 1.55 V for $Ir_2Sn_1O_x$-Ar increased to 3.0 mA $cm^{-2}$, which is higher than that of $Ir_2Sn_1O_x$ (1.2 mA $cm^{-2}$). Moreover, the smaller Tafel slope (49 mV $dec^{-1}$) and $R_{ct}$ (15.52 ohm) also indicated the superior OER activity of $Ir_2Sn_1O_x$-Ar compared with that of $Ir_2Sn_1O_x$. The OER activity of $Ir_2Sn_1O_x$-Ar was almost the same with that of $IrO_x$-Ar, but the Ir content was reduced due to the introduction of Sn. Therefore, the utilization of Ir in $Ir_2Sn_1O_x$-Ar increased and the activity of the Ir species was inherently improved. The high activity of $Ir_2Sn_1O_x$-Ar was analyzed. The $Q$ of $Ir_2Sn_1O_x$-Ar was 8.83 mC $cm^{-2}$, similar to that of $Ir_2Sn_1O_x$ (8.23 mC $cm^{-2}$), indicating that the enhanced activity of $Ir_2Sn_1O_x$-Ar does not come from an increase in the active surface area. In comparison with $Ir_2Sn_1O_x$, which is prepared by a single heat-treatment, there is sufficient time for the Ir and Sn species to interact and combine to form $Ir_2Sn_1O_x$-Ar during the first heat treatment at 500°C in Ar. As a result, a tighter combination between the Ir and Sn species in the final product and the corresponding enhanced synergistic effect will

produce high OER activity in $Ir_2Sn_1O_x$-Ar. The overpotential of $Ir_2Sn_1O_x$-Ar at 10 mA cm$^{-2}$ is 0.355 V, which is lower than that of meso-Sb-SnO$_2$/IrO$_2$ (50% IrO$_2$, ~0.38 V),[12] demonstrating the advantage of the support-free OER catalyst. Moreover, the overpotential of $Ir_2Sn_1O_x$-Ar at 1.0 mA cm$^{-2}$ is 0.30 V, which is lower than that of $Ir_{0.08}Ti_{0.92}O_2$ (0.33 V),[25] which may come from the higher porosity of $Ir_2Sn_1O_x$-Ar. In addition, the overpotential of $Ir_2Sn_1O_x$-Ar at 0.5 mA cm$^{-2}$ is 0.28 V, which is similar to that of 3-DOM IrO$_2$ (500°C, ~0.29 V),[22] leached-$Ir_{0.7}Co_{0.3}O_x$ (0.26 V)[6] and leached-$Ir_{0.7}Ni_{0.3}O_x$ (0.25 V)[26] with high porosity, but additional template removal and acid leaching processes were avoided in our method. Therefore, the material preparation strategy in this work provided a facile and efficient pathway to fabricate high-performance OER catalysts, which deserve further investigation and may well be applied in the future.
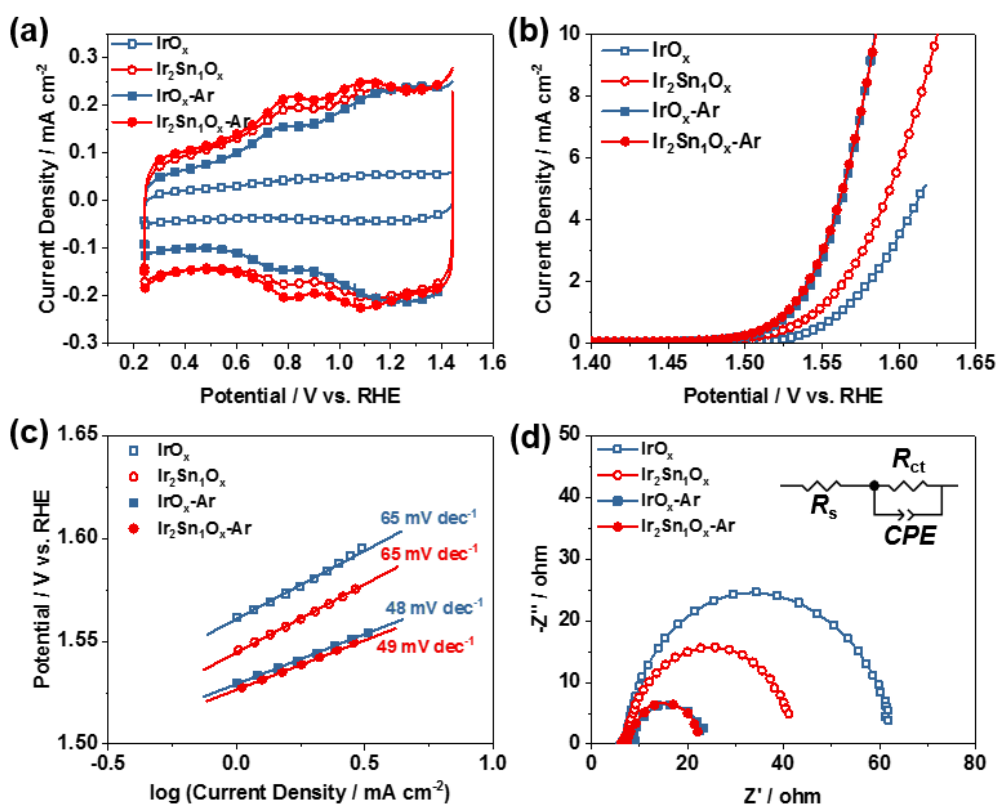


**Figure 8.** (a) CV curves, (b) OER polarization curves, (c) Tafel plots and (d) EIS spectra of $Ir_2Sn_1O_x$-Ar, IrO$_x$-Ar, $Ir_2Sn_1O_x$ and IrO$_x$ in 0.5 M H$_2$SO$_4$. The equivalent circuit of the EIS spectrum is shown in the inset of (d).

## 4. CONCLUSIONS

In this work, we provided a facile method to prepare Ir-Sn oxides in the form of a nanorod assembly with a large number of pores. Glucose and urea were used to prepare a deep eutectic solvent to dissolve IrCl$_3$ and SnCl$_2$. The heat-induced polymerization and expansion of glucose produced a GF with embedded Ir and Sn metal ions. During the following calcination, the presence of the GF inhibited the sintering of the catalyst, and the removal of the GF produced pores in the final product.

The –NH$_2$ groups in urea can form complexes with Ir and Sn metal ions, which is beneficial for the formation of an Ir-Sn binary oxide with uniform composition. The results of this study show that Ir$_2$Sn$_1$O$_x$ presented the best catalytic activity for the OER among the Ir-Sn oxides. Furthermore, an additional heat treatment of the metal-containing GF in Ar further increased the activity of the electrocatalyst. As a result, Ir$_2$Sn$_1$O$_x$-Ar presented a higher activity than that of Ir$_2$Sn$_1$O$_x$, which is identical to that of the mono-Ir oxide (IrO$_x$-Ar). The strategy described in this work may be applied in the development of other functional materials.

**References**

1.  J.H. Wang, W. Cui, Q. Liu, Z.C. Xing, A.M. Asiri and X.P. Sun, *Adv. Mater.*, 28 (2016) 215.
2.  J. Wang, F. Xu, H. Jin, Y. Chen and Y. Wang, *Adv. Mater.*, 29 (2017) 1605838.
3.  M. Carmo, D.L. Fritz, J. Merge and D. Stolten, *Int. J. Hydrogen Energy*, 38 (2013) 4901.
4.  L. Han, S. Dong and E. Wang, *Adv. Mater.*, 28 (2016) 9266.
5.  E. Antolini, *ACS Catal.*, 4 (2014) 1426.
6.  W. Hu, H. Zhong, W. Liang and S. Chen, *ACS Appl. Mater. Interfaces*, 6 (2014) 12729.
7.  Y. Pi, N. Zhang, S. Guo, J. Guo and X. Huang, *Nano Lett.*, 16 (2016) 4424.
8.  P. Mazúr, J. Polonský, M. Paidar and K. Bouzek, *Int. J. Hydrogen Energy*, 37 (2012) 12081.
9.  R.E. Fuentes, J. Farell and J.W. Weidner, *Electrochem. Solid-State Lett.*, 14 (2011) E5.
10. A.T. Marshall and R.G. Haverkamp, *Electrochim. Acta*, 55 (2010) 1978.
11. X. Wu and K. Scott, *Int. J. Hydrogen Energy*, 36 (2011) 5806.
12. J.L. Tong, Y. Liu, Q. Peng, W. Hu and Q. Wu, *J. Mater. Sci.*, 52 (2017) 13427.
13. V.K. Puthiyapura, M. Mamlouk, S. Pasupathi, B.G. Pollet and K. Scott, *J. Power Sources*, 269 (2014) 451.
14. A. Di Blasi, C. D'Urso, V. Baglio, V. Antonucci, A.S. Arico, R. Ornelas, F. Matteucci, G. Orozco, D. Beltran, Y. Meas and L.G. Arriaga, *J Appl Electrochem*, 39 (2009) 191.
15. A.T. Marshall, S. Sunde, M. Tsypkin and R. Tunold, *Int. J. Hydrogen Energy*, 32 (2007) 2320.
16. J.B. Cheng, H.M. Zhang, H.P. Ma, H.X. Zhong and Y. Zou, *Int. J. Hydrogen Energy*, 34 (2009) 6609.
17. M. Ito, Y. Murakami, H. Kaji, H. Ohkawauchi, K. Yahikozawa and Y. Takasu, *J. Electrochem. Soc.*, 141 (1994) 1243.
18. A. Marshall, B. Børresen, G. Hagen, M. Tsypkin and R. Tunold, *Mater. Chem. Phys.*, 94 (2005) 226.
19. S.D. Song, H.M. Zhang, X.P. Ma, Z.G. Shao, R.T. Baker and B.L. Yi, *Int. J. Hydrogen Energy*, 33 (2008) 4955.
20. W. Hu, P. Zhou, S. Xu, S.L. Chen and Q.H. Xia, *J. Mater. Sci.*, 50 (2015) 2984.
21. G.F. Li, H.M. Yu, W. Song, M.L. Dou, Y.K. Li, Z.G. Shao and B.L. Yi, *Chemsuschem*, 5 (2012) 858.
22. W. Hu, Y. Wang, X. Hu, Y. Zhou and S. Chen, *J. Mater. Chem.*, 22 (2012) 6010.
23. G. Li, H. Yu, X. Wang, S. Sun, Y. Li, Z. Shao and B. Yi, *Phys. Chem. Chem. Phys.*, 15 (2013) 2858.
24. G.F. Li, H.M. Yu, D.L. Yang, J. Chi, X.Y. Wang, S.C. Sun, Z.G. Shao and B.L. Yi, *J. Power Sources*, 325 (2016) 15.
25. Q. Wang, R. Wang and H.B. Xu, *Chem. J. Chin. Univ.*, 35 (2014) 1962.

26. S. Xu, S.L. Chen, L.H. Tian, Q.H. Xia and W. Hu, *J. Solid State Electrochem.*, 20 (2016) 1961